

Structural and dielectric properties of Sr_2TiO_4 from first principles

Craig J. Fennie and Karin M. Rabe

Department of Physics and Astronomy, Rutgers University, Piscataway, NJ 08854-8019

(Dated: October 26, 2018)

We have investigated the structural and dielectric properties of Sr_2TiO_4 , the first member of the $\text{Sr}_{n+1}\text{Ti}_n\text{O}_{3n+1}$ Ruddlesden-Popper series, within density functional theory. Motivated by recent work in which thin films of Sr_2TiO_4 were grown by molecular beam epitaxy (MBE) on SrTiO_3 substrates, the in-plane lattice parameter was fixed to the theoretically optimized lattice constant of cubic SrTiO_3 ($n=\infty$), while the out-of-plane lattice parameter and the internal structural parameters were relaxed. The fully relaxed structure was also investigated. Density functional perturbation theory was used to calculate the zone-center phonon frequencies, Born effective charges, and the electronic dielectric permittivity tensor. A detailed study of the contribution of individual infrared-active modes to the static dielectric permittivity tensor was performed. The calculated Raman and infrared phonon frequencies were found to be in agreement with experiment where available. Comparisons of the calculated static dielectric permittivity with experiments on both ceramic powders and epitaxial thin films are discussed.

PACS numbers: 77.22.Ch, 63.20.Dj, 61.66.Fn

I. INTRODUCTION

Nonstoichiometric SrTiO_3 resists the formation of point defects by forming crystallographic shear (CS) phases.¹ For excess SrO , these CS phases form the $\text{Sr}_{n+1}\text{Ti}_n\text{O}_{3n+1}$ Ruddlesden-Popper (RP) series. The structures of the members of the RP series can be viewed as a stacking of SrO -terminated SrTiO_3 perovskite [001] slabs with relative shifts of $(a_0/2)[110]$, the slabs in the n th member of the series having a thickness of n cubic perovskite lattice constants. This representation of the structure for $n = 1$ is shown in Fig. 1(a).

Considerable fundamental and practical interest in the RP series arises from the dielectric properties of its end member SrTiO_3 ($n = \infty$). Strontium titanate is an incipient ferroelectric with a high dielectric constant that can be readily tuned by applying a small DC bias. SrTiO_3 has low dielectric loss at microwave frequencies but a large temperature coefficient of dielectric constant (TCF). The prospect of “engineering” the properties of the constituent SrTiO_3 layers by varying n has stimulated the synthesis and study of the dielectric properties of various members of the RP series. Through the use of conventional ceramic processing techniques, single phase Sr_2TiO_4 ($n = 1$),^{1,2,3,4,5} $\text{Sr}_3\text{Ti}_2\text{O}_7$ ($n = 2$),^{1,3,4,5,6} and $\text{Sr}_4\text{Ti}_3\text{O}_{10}$ ($n = 3$),³ were formed. Recently, thin films of the first five members of the RP series were grown by molecular beam epitaxy (MBE) on SrTiO_3 substrates.^{8,9} Sr_2TiO_4 , $\text{Sr}_3\text{Ti}_2\text{O}_7$, and $\text{Sr}_4\text{Ti}_3\text{O}_{10}$ were found to be nearly single phase while $\text{Sr}_5\text{Ti}_4\text{O}_{13}$ and $\text{Sr}_6\text{Ti}_5\text{O}_{16}$ films showed noticeable antiphase boundaries and intergrowth defects.⁹ The dielectric properties of the $n = 1, 2$, and ∞ ceramic samples have been characterized by various groups.^{4,5,7,10} The dielectric properties of the $n = 3$ and 4 ceramic samples have also been studied but these were believed not to be single phase.⁵ It was found that SrTiO_3 had both the highest dielectric constant, ϵ_r , and the largest TCF of the RP series. Conversely, Sr_2TiO_4

was found to have the lowest ϵ_r of the series but also the lowest TCF (an order of magnitude smaller than SrTiO_3) while having a dielectric loss comparable to SrTiO_3 . For thin films, Haeni *et al.*⁹ performed low frequency and microwave experiments to measure the dielectric permittivity of Sr_2TiO_4 and of $\text{Sr}_3\text{Ti}_2\text{O}_7$, to be discussed below.

Here we take the first step in understanding the dielectric behavior of the $\text{Sr}_{n+1}\text{Ti}_n\text{O}_{3n+1}$ Ruddlesden-Popper (RP) series from first principles by presenting our study of the structural and dielectric properties of Sr_2TiO_4 ($n = 1$) using density functional theory (DFT) structural optimization as well as density functional perturbation theory (DFPT). DFT and DFPT have proved to be useful tools in investigating the structure, dynamical and dielectric properties of metals and insulators, including complex oxides (see Ref. 11 for a review). In Section II we give the details of our DFT/DFPT calculations and describe various constraints that we imposed on the Sr_2TiO_4 structure. In Section III the results of our calculations for the ground-state structural parameters, Born effective charges, zone-center phonons and electronic and static dielectric permittivity tensors at $T=0$ are presented and compared with experiment. In Section IV we discuss the sensitivity of the dielectric response to structural constraints, and through comparison with SrTiO_3 , explore the key role played by the Ti-O chain geometry¹² in the dielectric response and its anisotropy in the RP phases. Finally, in Section V we summarize our results and main conclusions.

II. METHOD

A. First principles calculations

First-principles density-functional calculations were performed within the local density approximation (LDA) as implemented in the ABINIT package.¹³ The exchange-

correlation energy is evaluated using the Teter rational polynomial fit to the Ceperley-Alder electron-gas data.¹⁴ Teter extended norm-conserving pseudopotentials were used with Ti(3s 3p 4s 3d), Sr(4s 4p 5s), and O(2s 2p) levels treated as valence states. The electronic wavefunctions were expanded in plane waves up to a kinetic energy cutoff of 35 Ha. Integrals over the Brillouin zone were approximated by sums on a $6 \times 6 \times 2$ mesh of special k -points.¹⁵

B. Structural Constraints

We first performed full optimization of the lattice parameters and internal coordinates in the reported structure of Sr_2TiO_4 ,² the body-centered tetragonal K_2NiF_4 structure (space group $I4/mmm(D_{4h}^{17})$, with the primitive unit cell containing one formula unit as shown in Fig. 1. Ti atoms occupy Wyckoff position (2a), O_x and O_y atoms (4c), and Sr and O_z atoms (4e), the latter with one free parameter (displacement along \hat{z}) each (see Table I). This yields the predicted structure under zero stress, roughly corresponding to bulk ceramic powders and relaxed epitaxial films. The structural relaxation was performed using a modified Broyden-Fletcher-Goldfarb-Shanno (BFGS) algorithm¹⁶ to optimize the volume and atomic positions, followed by an optimization of the c/a ratio. This procedure was repeated to ensure convergence. The residual Hellmann-Feynman forces were less than 2 meV/Å. A second structure was considered to investigate the effects of epitaxial strain induced by the SrTiO_3 substrate on a fully coherent thin film. With the same space group, we fixed the in-plane lattice parameter to that of SrTiO_3 calculated within the present theory ($a = 3.846\text{Å}$),¹⁷ while optimizing the other structural parameters: the c lattice constant and displacements along [001]. This was followed by ionic relaxation until the residual Hellmann-Feynman forces were less than 1 meV/Å.

The next section will show that the fully optimized lattice parameters are underestimated relative to the experimental values, a common feature in LDA calculations.¹⁸ To investigate whether our calculations of the dielectric response of Sr_2TiO_4 are sensitive to this underestimation of the volume, two additional structures were considered. First, with the same space group, we optimized all internal coordinates fixing both the a and c lattice constants to values obtained by uniformly expanding the lattice constant of the in-plane constrained structure using the measured thermal expansion coefficient of SrTiO_3 ^{19,20} ($\alpha \approx 7 \times 10^{-6}/\text{K}$) and a temperature increase of 300 K. We also optimized internal coordinates fixing both the a and c lattice constants to the values experimentally obtained for the thin film sample. In both structures the ions were relaxed until the residual Hellmann-Feynman forces were less than 1 meV/Å.

C. Linear response calculations

Linear response methods provide an efficient means for computing quantities that can be expressed as derivatives of the total energy E with respect to a perturbation, such as that produced by displacement $u_{i\alpha}$ of an atom or a homogeneous electric field \mathcal{E} . Examples computed in this work include the force constant matrix elements

$$\left. \frac{\partial^2 E}{\partial u_{i\alpha} \partial u_{j\beta}} \right|_0$$

where $u_{i\alpha}$ is the displacement of atom i in cartesian direction α from its position in the equilibrium crystal structure, the Born effective charge tensor

$$Z_{i\alpha\beta}^* = - \frac{\partial^2 E}{\partial d_{i\alpha} \partial \mathcal{E}_\beta}$$

where $d_{i\alpha}$ is the uniform displacement of the atomic sublattice i in cartesian direction α from its position in the equilibrium unit cell, with derivatives taken in zero macroscopic field, and the electronic susceptibility tensor

$$\chi_{\alpha\beta} = - \frac{\partial^2 E}{\partial \mathcal{E}_\alpha \partial \mathcal{E}_\beta}$$

which is related to the electronic dielectric permittivity tensor ϵ_∞ by $\epsilon_\infty = 1 + 4\pi\chi$. In this work, we compute these derivatives using the variational formulation of density-functional perturbation theory (DFPT), implemented in the ABINIT package.^{13,21,22}

The static dielectric permittivity tensor ϵ_0 can be obtained directly from the quantities computed by DFPT. In general the static dielectric permittivity tensor of a nonpolar material can be written^{23,24} as the sum of the electronic dielectric permittivity tensor ϵ_∞ and a sum of contributions $\Delta\epsilon_m$ from each of the zone-center polar modes m :

$$\epsilon_{\alpha\beta}^0 = \epsilon_{\alpha\beta}^\infty + \sum_m \Delta\epsilon_{m,\alpha\beta} \quad (1)$$

where $\Delta\epsilon_m$ is given by^{25,26}

$$\Delta\epsilon_{m,\alpha\beta} = \frac{4\pi e^2}{M_0 V} \frac{\tilde{Z}_{m\alpha}^* \tilde{Z}_{m\beta}^*}{\omega_m^2} \quad (2)$$

Here, V is the volume of the primitive unit cell and M_0 is a reference mass taken as 1 amu. $\frac{4\pi e^2}{M_0 V} \tilde{Z}_{m\alpha}^* \tilde{Z}_{m\beta}^*$ can be thought of as an effective plasma frequency, $\Omega_{p,m}^2$, of the m^{th} normal mode,^{27,28} while ω_m is the frequency of vibration of normal mode m . $\tilde{Z}_{m\alpha}^*$, which has been referred to as a mode effective charge,^{31,32,33} is given by

$$\tilde{Z}_{m\alpha}^* = \sum_{i\gamma} Z_{\alpha\gamma}^*(i) \left(\frac{M_0}{M_i} \right)^{1/2} \xi_m(i\gamma) \quad (3)$$

where ξ_m is the dynamical matrix eigenvector; the corresponding real space eigendisplacement of atom i along β

is given by $U_m(i\beta) = \xi_m(i\beta)/M_i^{1/2}$.²⁹ Thus we see that large lattice contributions to the static dielectric permittivity tensor are expected if the relevant mode frequencies are very low and/or if the effective plasma frequencies are large (reflecting large mode effective charges).

This formalism has been applied in a first-principles context in numerous calculations of the zero-temperature static dielectric response (for a review, see Ref. 30) in simple and complex oxides. For example, recent calculations for zircon (ZrSiO_4)²³ and zirconia (ZrO_2)^{24,31} yield good agreement with experiment.

III. RESULTS

A. Crystal Structure of Sr_2TiO_4

The reported crystal structure of Sr_2TiO_4 can also be viewed as a stacking of TiO_2 and SrO planes along $[001]$ as shown in Fig. 1(b), the stacking sequence being TiO_2 - SrO - SrO where the second SrO layer is shifted with respect to the previous SrO layer by $\frac{1}{2}a_0$ along $[110]$. In previous work (Ref. 35), the internal structural parameters are presented as u' and v , the distance between TiO_2 and SrO planes and between successive SrO planes, respectively, and δ , the distance along c between Sr and O in the same SrO layer, which quantifies the “rumpling” of the layer.

In Table II we present the theoretical lattice parameters for the structures discussed in Section II and compare them with the experimental values for ceramic samples^{2,4,52} and for thin films epitaxially grown on SrTiO_3 ($a=3.905\text{\AA}$) substrates.^{8,9} The lattice constants of the fully relaxed structure, Table II(a), are smaller than the measured lattice constants of the ceramic powder. Specifically, the a lattice parameter was calculated to be less than experiment by 1.5%, which is within the error typically associated with the LDA, while the c lattice parameter is underestimated by 2.2%. The smaller value of c measured for the thin film samples reduces this discrepancy to 1.1%. There is considerable rumpling of the SrO layers, $\delta_{\text{SrO}} = 0.05a_0$. This rumpling is such that the O_z and Sr atoms move in a direction away from and towards the TiO_2 layers, resulting in a Ti-O_z bond slightly larger (2.9%) than the Ti-O_y (or equivalently Ti-O_x) bond. As pointed out by Noguera, Ruddlesden and Popper had assumed that this rumpling was equal to zero. The present study supports the previous calculation³⁵ by finding a nonzero rumpling. The experimental work of Venkateswaran *et al.*⁵² also suggested a nonzero rumpling of the SrO layer ($\delta_{\text{SrO}}=0.10$),³⁸ but found that the Ti-O_z bond is shorter than the Ti-O_y bond.

Next, we consider the structure in which we constrained the in-plane lattice constant to that of theoretical SrTiO_3 ($a = 3.846\text{\AA}$), Table II(b). This places the system under tensile in-plane stress equal to that of an experimental sample of Sr_2TiO_4 coherently matched to SrTiO_3 (lattice mismatch 0.6%). As can be seen in Ta-

ble II, this has almost no effect on the optimized values of the other structural parameters, including c .

Finally, we consider the optimized structural parameters for the two expanded structures. The slight thermal expansion of the in-plane constrained structure has a correspondingly slight effect on the internal parameters, while the expanded c of the experimental thin film structure has a larger effect. We see that a roughly homogeneous expansion of the lattice, i.e. column (a) \rightarrow (d) and (b) \rightarrow (c), decreases the rumpling of the SrO layer.

B. Born Effective Charge Tensors

In the Sr_2TiO_4 structure, the site symmetries of the Ti atom, occupying Wyckoff position 2a, and the O_z and Sr atoms, both occupying Wyckoff position 4e, are tetragonal, while that of the O_x and O_y atoms, Wyckoff position 4c, is orthorhombic. As a result, all Z^* 's are diagonal with two ($Z^*(\text{Ti})$, $Z^*(\text{O}_z)$, and $Z^*(\text{Sr})$) and three ($Z^*(\text{O}_y)$ and $Z^*(\text{O}_x)$) independent components. Table III displays the diagonal components of the calculated Born effective charge tensors in Sr_2TiO_4 for the four structures considered. We see that the Z^* 's are relatively insensitive to the various volume and strain constraints imposed, consistent with what was shown for isotropic volume changes in BaTiO_3 ³⁹ and for pure tetragonal strain in KNbO_3 .⁴⁰ Also, we note an anomalously large value for $Z_{xx}^*(\text{Ti}) = Z_{yy}^*(\text{Ti})$ (nominal charge +4) and for $Z_{xx}^*(\text{O}_x) = Z_{yy}^*(\text{O}_y)$ (nominal charge -2), these being the components of the Z^* 's corresponding to motion parallel to the Ti-O bond along a direction in which the infinite Ti-O chains have been preserved. In contrast, the anomalous parts of $Z_{zz}^*(\text{Ti})$ and $Z_{zz}^*(\text{O}_z)$, which again correspond to motion parallel to the Ti-O bond, but along $[001]$ where the Ti-O bonds do not form continuous chains, are found to be less than half of those along the continuous Ti-O chain.

C. Phonon Frequencies at Γ

For the Sr_2TiO_4 structure, group-theoretical analysis predicts that the 18 zone-center optic modes transform according to the following irreducible representations

$$\Gamma_{\text{optic}} = 2A_{1g} \oplus 2E_g \oplus 3A_{2u} \oplus 4E_u \oplus B_{2u} \quad (4)$$

of which the A_{1g} and E_g modes are Raman active, the A_{2u} and E_u modes are infrared active, and the B_{2u} mode is neither Raman nor infrared active. By using projection operator methods, it can be shown that the A_{1g} , A_{2u} , and B_{2u} modes involve motion along $[001]$ while in the E_g and E_u modes, atoms move along $[100]$ and $[010]$. A complete listing of the symmetry adapted lattice functions is given in Refs. 41 and 42.

Table IV displays our calculated frequencies and mode assignments for the four structures considered. Compar-

ing the calculated phonon frequencies for the fully relaxed structure (a) with those measured by Burns *et al.* on ceramic samples,⁴¹ also given in Table IV, we find excellent agreement. The calculations allow us to confirm the mode assignments of the $A_{2u}(TO1)$ and $E_u(TO3)$: Burns' suggestion of assigning the lower mode at 242 cm^{-1} A_{2u} symmetry and the higher mode at 259 cm^{-1} E_u symmetry appears to be correct. In addition, Burns' assessment that the strong LO feature at $\approx 440\text{ cm}^{-1}$ in the measured reflectivity spectra was "probably" due to both a $A_{2u}(LO)$ and a $E_u(LO)$ mode is consistent with our calculations, where we found $A_{2u}(LO) = 479\text{ cm}^{-1}$ and $E_u(LO) = 451\text{ cm}^{-1}$.⁴³ In fact an average of these two frequencies is within 2 cm^{-1} of the quoted value 467 cm^{-1} . Finally, we obtain the frequencies of four modes that could not be separately identified in the experiment, namely the $A_{2u}(TO2)$ mode at 378 cm^{-1} , $A_{2u}(LO)$ mode at 252 cm^{-1} , the $E_u(TO4)$ mode at 611 cm^{-1} , and the B_{2u} mode at 303 cm^{-1} .

In Table V we give the normalized dynamical matrix eigenvectors for the fully relaxed structure (a). We see that the lowest frequency $A_{2u}(TO1)$ and $E_u(TO1)$ modes involve Sr atoms moving against a fairly rigid TiO_6 octahedron, with larger deformation of the octahedron for the E_u mode. The highest frequency $A_{2u}(TO3)$ and $E_u(TO4)$ modes each involve large distortions of the oxygen octahedra with the apical oxygens moving against the planar oxygens in the A_{2u} mode and a corresponding distortion for the E_u mode. The calculated $A_{2u}(TO2)$ mode involves Ti atoms moving against a nearly rigid oxygen octahedron, giving rise to a relatively large mode effective charge. Finally, the $E_u(TO2)$ mode, characterized by Burns *et al.* as a weak infrared active mode, has displacements of O_y and O_z very close to those of the triply degenerate silent mode in the cubic perovskite. These patterns are substantially different from those obtained in model calculations of the lattice dynamics of K_2ZnF_4 ,⁴⁴ used by Burns to characterize the eigenvectors of Sr_2TiO_4 , especially for the highest frequency $A_{2u}(TO3)$ and $E_u(TO4)$ modes and the $A_{2u}(TO2)$ mode.

The effective plasma frequencies (Sec. II C) are reported in Table VI. There is relatively little variation among the different modes of the same symmetry in the same structure, with $\Omega_{p,m} \approx 400\text{ cm}^{-1}$ and 800 cm^{-1} for the A_{2u} and E_u respectively, and even less variation with changes in the structure. The largest calculated effective plasma frequency is obtained for the $A_{2u}(TO2)$ mode. While the corresponding oscillator strength, which goes like $\Omega_{p,m}^2$, should make this the most prominent mode in a single-crystal infrared study, it was not separately identified in the ceramic sample of Burns. In ceramics, while the reststrahlen bands do not overlap for modes transforming as the same irreducible representation, the A_{2u} modes can overlap the E_u and vice versa. In fact we see that not only the $A_{2u}(TO2)$ mode, but also a second high-oscillator strength mode, $E_u(TO4)$, not identified in the measurements of Burns, lie in the middle of a wide reststrahlen band of the other symmetry type. As noted

by Burns, this would undoubtedly complicate the interpretation of the reflectivity spectrum and may explain why neither of these modes were identified.

D. Dielectric Permittivity Tensors

Here we present our calculation of the static dielectric permittivity tensor ϵ_0 for the structures considered in Table II. By the symmetry of the Sr_2TiO_4 structure we see that the tensors are diagonal and have two independent components, along directions parallel to and perpendicular to the TiO_2 layers. In Table VII we display the results of our calculations for these three tensors (ϵ_∞ , ϵ_{ionic} , and ϵ_0) for Sr_2TiO_4 under the various structural constraints previously discussed (see the caption of Table II). It can be seen that the static dielectric permittivity tensor is quite anisotropic, with the in-plane components nearly 3 times as large as the component along $[001]$.

To improve our understanding of this anisotropy we examine the contribution to ϵ_{ionic} from individual phonon modes. In Table VI we show the effective plasma frequency, $\Omega_{p,m}$, and the contribution to the static dielectric permittivity for each IR-active phonon mode, equal to $\frac{\Omega_{p,m}^2}{\omega_m^2}$. The A_{2u} and the E_u modes contribute to the components of ϵ_0 along directions perpendicular and parallel to the TiO_2 layers, respectively. We see that the dominant mode contributing to the rather large anisotropy is the $E_u(TO1)$ mode, while the largest $\Omega_{p,m}$ is associated with the $A_{2u}(TO2)$ mode. In fact the effective plasma frequency of the $A_{2u}(TO2)$ mode is $\sim 40\%$ larger than that of the $E_u(TO1)$ mode. The fact that the frequency of this $A_{2u}(TO2)$ mode is more than twice that of the soft $E_u(TO1)$ mode explains its relatively small contribution to the dielectric permittivity tensor.

Finally, to compare the calculated dielectric permittivity tensors with the measured dielectric constant of the ceramic samples, ϵ_r , we compute an orientational average, $\epsilon_{\text{average}}$, of our calculated results. From Table VII we see that $\epsilon_{\text{average}} = 38$ for the fully-relaxed structure agrees quite well with $\epsilon_r = 34 - 38$ measured by the various groups. The comparison with the thin film results is more problematic and will be discussed in the next section.

IV. DISCUSSION

In this section, we discuss the main features of the $T=0$ dielectric response of Sr_2TiO_4 and its relationship to that of SrTiO_3 . We show that the anisotropy and sensitivity to changes in the lattice constants through epitaxial strain and thermal expansion can be understood by focusing on the Ti-O chains and chain fragments. Finally, we discuss the comparison of the results of our calculations to available experimental data.

As noted in the previous section, the static dielectric

tensor of Sr_2TiO_4 is rather anisotropic, with the response in the planes of the layers about three times greater than the response perpendicular to the layers. This can be understood by analyzing the Ti-O chains. In SrTiO_3 , the large dielectric response can be directly linked to the presence of infinite Ti-O chains running in all three cartesian directions, with anomalously large Born effective charges and low frequencies for modes with Ti displacing relative to O along the chain^{55,56} (see Table VIII). In Sr_2TiO_4 the infinite Ti-O chains lying in the TiO_2 planes are preserved, while the Ti-O chains along [001] are broken into short O-Ti-O segments by the relative shift of the SrO-terminated perovskite slabs (see Figure 1(c)). Correspondingly, as can be seen in Table III the Z^* 's in Sr_2TiO_4 for Ti and O displacing along the infinite chains in the TiO_2 layers, $Z_{yy}^*(\text{Ti})$ ($Z_{xx}^*(\text{Ti})$) and $Z_{yy}^*(\text{O}_y)$ ($Z_{xx}^*(\text{O}_x)$), are only slightly smaller than those of SrTiO_3 .⁴⁵ In contrast, the breaking of the Ti-O chains into O-Ti-O segments along [001] has a dramatic effect on the anomalous component of the Ti and O Born effective charges for motion along the segment, $Z_{zz}^*(\text{Ti})$ and $Z_{zz}^*(\text{O}_z)$, reducing them by over a factor of 2. While it is true that the local anisotropy caused by the somewhat larger Ti-O_z bond length compared with the Ti-O_y bond length will also reduce the corresponding Born effective charges, this is a much weaker effect as suggested by the following calculation. We fixed the Ti-O_z distance to that of the Ti-O_y bond length of structure (b) (where the in-plane plane lattice parameter was fixed to the lattice constant of SrTiO_3), creating a structure whereby the Ti-O distances are equal in all three cartesian directions. The Born effective charges along [001] were found to increase, but only slightly ($Z_{zz}^*(\text{Ti})=5.29$ and $Z_{zz}^*(\text{O}_z)=-3.80$).

This reduction of the anomalous component of the Born effective charges is quite similar to the reduction of the Z^* 's observed in BaTiO_3 due to the ferroelectric transition. Indeed, Ghosez *et al.*^{12,39} found that $Z^*(\text{Ti}) = 7.29$ and $Z^*(\text{O}_{\parallel}) = -5.75$ in cubic BaTiO_3 while in the tetragonal phase they found $Z_{yy}^*(\text{Ti}) = 6.94$, $Z_{yy}^*(\text{O}_y) = -5.53$, $Z_{zz}^*(\text{Ti}) = 5.81$ and $Z_{zz}^*(\text{O}_z) = -4.73$. It was explained that this reduction of the Z^* 's going from the cubic to the tetragonal phase resulted from the displacement of the Ti atom along the ferroelectric axis, resulting in a series of long-short Ti-O bonds thereby "breaking" the Ti-O chains.¹² In Sr_2TiO_4 this breaking of the Ti-O chains can be thought of as being caused not by alternating Ti-O bond lengths along a given direction, but by the shift of the SrO-terminated SrTiO_3 slabs, resulting in a SrO-SrO anti-phase boundary perpendicular to [001] as discussed in Sec. III A. Finally, this breaking of the chains in Sr_2TiO_4 is arguably a much "stronger" effect than the cubic to tetragonal transition in BaTiO_3 , as evidenced by the greater reduction of the Born effective charges along [001].

The breaking of the [001] Ti-O chains into segments lowers the dielectric response relative to SrTiO_3 also by stiffening the low-frequency mode associated with relative displacement of Ti and O along the chains. The

in-plane E_u (TO1) mode in Sr_2TiO_4 for the fully relaxed structure (a) is at 148 cm^{-1} (134 cm^{-1} for the structure with in-plane lattice constant fixed to SrTiO_3 (b)) comparable to our calculated value of 103 cm^{-1} for SrTiO_3 , while the corresponding out-of-plane A_{2u} (TO2) mode is at 378 cm^{-1} for structure (a) (391 cm^{-1} for structure (b)). As we discussed in the previous section, the large anisotropy is almost completely accounted for by the large $\Delta\epsilon_m$ of the in-plane E_u (TO1) mode as shown in Table VI.

The topology of the Ti-O chains thus appears to be much more important than the bond lengths and the details of the geometry. Indeed, our calculations show that the dielectric permittivity tensor of Sr_2TiO_4 is not very sensitive to an in-plane tensile strain. From Table VII we see that $\epsilon_{\text{average}}$ for the fully-relaxed structure (a) and for the structure with the in-plane lattice constant constrained to the theoretical SrTiO_3 value (b) only differ by $\sim 15\%$. Also, we see that this difference originates from the component of ϵ_{ionic} along in-plane directions while the lattice contribution to the dielectric permittivity tensor along [001] remains relatively constant. In particular, we see that ϵ_{ionic} along directions in which the Ti-O chains were preserved is relatively more sensitive to a fixed strain than along directions in which these chains were broken. In fact this sensitivity can be attributed to a single $E_u(\text{TO1})$ mode where it can be seen that the sum of the contributions to ϵ_{ionic} from the remaining $E_u(\text{TO})$ modes remains nearly constant for all the structures considered. As was pointed out in Sec. III D this $E_u(\text{TO1})$ mode also contributes predominately to the rather large anisotropy of the static dielectric permittivity tensor. Thus, the difference in response between fully coherent and fully relaxed films is expected to be relatively insignificant, unlike the case of epitaxial thin films of SrTiO_3 , in which the induced strain would influence the lattice dynamics and presumably could have significant effect on the dielectric properties.^{46,47} In addition, this insensitivity should reduce the TCF, especially for ϵ_{33} .

Anisotropy of the dielectric tensor has not been previously experimentally determined in Sr_2TiO_4 , though measurements have been carried out for single crystals of some isostructural oxides CaYAlO_4 , CaNdAlO_4 , and LaSrAlO_4 .⁴⁸ In the latter case, the anisotropy is very small (and in the case of LaSrAlO_4 , the out-of-plane component of the dielectric tensor, $\epsilon_{33} = 20.02$, is slightly greater than the in-plane component $\epsilon_{11} = \epsilon_{22} = 16.81$). The absence of a large in-plane response in these materials highlights the unique physics of the Ti-O chain.

The anisotropy of the dielectric tensor is an important factor to be taken into consideration when comparing the computed dielectric response with experiment, and indeed in correctly interpreting experimental measurements. For ceramics, anisotropy of the single crystal response can give a range of values for the measured dielectric response, depending on the size, shape and interaction of the grains. In the single crystal films,

the anisotropy complicates the interpretation of the microwave microscope method of determining the dielectric response. The effective dielectric constant obtained by this technique is in fact an average of the dielectric tensor components determined by the field distribution near the probe, which is itself determined by the anisotropic dielectric response. While an exact value requires detailed modeling of the field configuration, the expectation is that the measured value should be an average weighted in favor of the high dielectric response components. Thus, the value $\epsilon_{eff} = 44$ obtained by Haeni⁹ is not ϵ_{33} , but is a weighted average of the three components, in accordance with our calculations. The agreement of this ϵ_{eff} with the low-frequency electronic measurement is apparently coincidental. The latter measurement determines ϵ_{33} , but at low frequencies it is not unusual for additional extrinsic contributions to raise the value of the dielectric response.

V. SUMMARY

Our calculation of the static dielectric tensor of Sr_2TiO_4 provides valuable information, not previously

available, about the anisotropy of the response. This anisotropy is key to interpreting the available experimental data on the dielectric response of ceramic and thin film samples. We identify a dominant role played by Ti-O chains in the lattice contribution to the response, which allows us to understand the anisotropy. This picture should generalize to higher RP phases of Sr-Ti-O, and further could be useful in tailoring the dielectric response of other perovskite-based systems.

Acknowledgments

The authors would like to acknowledge valuable discussions with Darrel Schlom, David Vanderbilt, and Morrel Cohen. This work was supported by NSF-NIRT DMR-0103354.

-
- ¹ R. J. D. Tilley, J. of Solid State Chem. **21**, 293 (1977).
 - ² S. N. Ruddlesden and P. Popper, Acta Cryst. **10**, 538 (1957).
 - ³ G. McCarthy, W. R. White, and R. Roy, J. Am. Ceram. Soc. **52**, 463 (1969).
 - ⁴ J.H. Sohn, Y. Inaguma, M. Itoh, and T. Nakamura, Ferroelectrics **166**, 149 (1995); Mater. Sci. Eng. B **41** 50 (1996).
 - ⁵ P. L. Wise, I. M. Reaney, W. E. Lee, T. J. Price, D. M. Iddles, D. S. Cannell, J. of the Eur. Ceram. Soc. **21**, 2629 (2001); **21**, 1723 (2001); J. Mater. Res. **17**, 2033 (2002).
 - ⁶ S. N. Ruddlesden and P. Popper, Acta Cryst. **11**, 54 (1958).
 - ⁷ W. Kwestroo and H. A. M. Paping, J. Am. Ceram. Soc. **42**, 292 (1959).
 - ⁸ W. Tian, X. Q. Pan, J. H. Haeni, and D. G. Schlom, J. Mater. Res. **16**, 2013 (2001).
 - ⁹ J. H. Haeni, C. D. Theis, D. G. Schlom, W. Tian, X. Q. Pan, H. Chang, I. Takeuchi, and X. D. Xiang, Appl. Phys. Lett. **78**, 3292 (2001).
 - ¹⁰ T. Nakamura, P.-H. Sun, Y. J. Shan, Y. Inaguma, M. Itoh, I.-S. Kim, J.-H. Sohn, M. Ikeda, T. Kitamura, H. Kona-gaya, Ferroelectrics **196**, 205 (1997).
 - ¹¹ S. Baroni, S. de Gironcoli, A. Dal Corso, and P. Giannozzi, Rev. Mod. Phys. **73**, 515 (2001).
 - ¹² Ph. Ghosez, J.-P. Michenaud, and X. Gonze, Phys. Rev. B **58**, 6224 (1998).
 - ¹³ ABINIT is a common project of the Université Catholique de Louvain, Corning Incorporated and other contributors, see the URL <http://www.mapr.ucl.ac.be/ABINIT>. It relies on an efficient fast fourier transform algorithm (Ref. 49) for the conversion of wavefunctions between real and reciprocal space, on the adaptation to a fixed potential of the band-by-band conjugate gradient method (Ref. 50), and on a potential-based conjugate-gradient algorithm for the determination of the self-consistent potential (Ref. 51). Technical details on the computation of responses to atomic displacements and homogeneous electric fields can be found in Ref. 21, while Ref. 22 presents the subsequent computation of dynamical matrices, Born effective charges, dielectric permittivity tensors, and interatomic force constants.
 - ¹⁴ D. M. Ceperley and B. J. Alder, Phys. Rev. Lett. **45**, 566 (1980).
 - ¹⁵ H. J. Monkhorst and J. D. Pack, Phys. Rev. B **13**, 5188 (1976); *ibid.*, Phys. Rev. B **16**, 1748 (1977).
 - ¹⁶ J. Schlegel, Comp. Chem. **3**, 214 (1982)
 - ¹⁷ Calculations were performed on $6 \times 6 \times 6$ grid at an energy cutoff of 45 Ha, following the approach described in Section II A.
 - ¹⁸ D. Vanderbilt, Current Opinions in Solid State and Materials Science **2**, 701 (1997).
 - ¹⁹ Na Sai and David Vanderbilt, Phys. Rev. B **62**, 13942 (2000).
 - ²⁰ F.W. Lytle, J. Appl. Phys. **35**, 2212 (1964).
 - ²¹ X. Gonze, Phys. Rev. B **55**, 10337 (1997).
 - ²² X. Gonze and Ch. Lee, Phys. Rev. B **55**, 10355 (1997).
 - ²³ G.-M. Rignanese, X. Gonze, and A. Pasquarello, Phys. Rev. B **63**, 104305 (2001).
 - ²⁴ G.-M. Rignanese, F. Detraux, X. Gonze, and A. Pasquarello, Phys. Rev. B **64**, 134301 (2001).
 - ²⁵ M. Born and K. Huang, *Dynamical Theory of Crystal Lattices*, Oxford University Press, Oxford, 1954.
 - ²⁶ A. A. Maradudin, E. W. Montroll, G. H. Weiss, and I. P. Ipatova, in Solid State Physics: Advances in Research and Applications, edited by H.E. Ehrenreich, F. Seitz, and D. Turnbull (Academic, New York, 19971), Suppl.3, Chap.4.
 - ²⁷ J.M. Ziman, *Principles of the Theory of Solids*, Cambridge

- University Press, Second Edition 1972.
- ²⁸ D.Y. Smith, in *Handbook of Optical Constants of Solids*, E.D. Palik Ed. (Academic Press, New York, 1985), pp. 35-68.
 - ²⁹ The mode effective charge, if defined as the constant of proportionality between the induced polarization and a real-space eigendisplacement is given by $\sum_{i\gamma} Z_{\alpha\gamma}^*(i) U_m(i\gamma) / [\sum_{i\gamma} U_m^*(i\gamma) U_m(i\gamma)]^{\frac{1}{2}}$.
 - ³⁰ U. V. Waghmare and K. M. Rabe, to appear.
 - ³¹ X. Zhao and D. Vanderbilt, Phys. Rev. B, **61**, 075105 (2002).
 - ³² X. Zhao and D. Vanderbilt, Phys. Rev. B, **65**, 233106 (2002).
 - ³³ E. Cockayne and B. Burton, Phys. Rev. B, **62**, 3735 (2000).
 - ³⁴ T. Suzuki and M. Fujimoto, J. of Appl. Phys. **89**, 5622 (2001).
 - ³⁵ Claudine Noguera, Phil. Mag. Lett. **80**, 173 (2000).
 - ³⁶ M. A. McCoy, R. W. Grimes, and W. E. Lee, Phil. Mag. A **75**, 833 (1997).
 - ³⁷ K. R. Udayakumar and A. N. Cormack, Comm. Am Ceram. Soc. **71**, C-469 (1988).
 - ³⁸ This assumes a c-axis lattice parameter ($c=12.60\text{\AA}$) equal to that previously reported in the literature for ceramic samples. Note, the c-axis lattice parameter is missing from their paper.
 - ³⁹ Ph. Ghosez, X. Gonze, Ph. Lambin, and J.-P. Michenaud, Phys. Rev. B **51**, 6765 (1995).
 - ⁴⁰ C.-Z. Wang, R. Yu, and H. Krakauer, Phys. Rev. B **54**, 11161 (1996).
 - ⁴¹ G. Burns, F. H. Dacol, G. Kliche, W. Konig, and M. W. Shafer, Phys. Rev. B **37**, 3381, (1988).
 - ⁴² G. Burns, F. H. Dacol, and M. W. Shafer, Solid State Commun. **62**, 687 (1987).
 - ⁴³ In Table II of the Ref.⁴¹, the A_{2u} mode and the E_u mode given rise to the strong LO feature at $\approx 440\text{ cm}^{-1}$ was each assigned a value of 467 cm^{-1} .
 - ⁴⁴ H. Rauh and R. Geick, Phys. Stat. Sol. (b) **127**, 55 (1985).
 - ⁴⁵ The hybridization of the Ti $3d$ and O $2p$ states has been shown to be the origin of the anomalous Born effective charges (BECs) in the perovskites⁵³. Because one expects this hybridization, or the rate of change of this hybridization³⁹, to depend on the length of the Ti-O bond we should compare BECs in SrTiO_3 and Sr_2TiO_4 at the same bond length.
 - ⁴⁶ S. Hyun and K. Char, Appl. Phys. Lett. **79**, 254 (2001).
 - ⁴⁷ A.R. James and X.X. Xi, J. of Appl. Phys. **92**, 6149 (2002).
 - ⁴⁸ R.D. Shannon, R.A. Oswald, J.B. Parise, B.H.T. Chai, P. Byszewski, A. Pajczkowska, and R. Sobolewski, J. of Solid State Chem. **98**, 90 (1992).
 - ⁴⁹ S. Goedecker, SIAM J. on Scientific Computing **18**, 1605 (1997).
 - ⁵⁰ M. C. Payne, M. P. Teter, D. C. Allan, T. A. Arias and J. D. Joannopoulos, Rev. Mod. Phys. **64**, 1045 (1992).
 - ⁵¹ X. Gonze, Phys. Rev. B **54**, 4383 (1996).
 - ⁵² U. Venkateswaran, K. Strossner, K. Syassen, G. Burns, and M. W. Shafer, Solid State Commun. **64**, 1273 (1987).
 - ⁵³ M. Posternak, R. Resta, and A. Baldereschi, Phys. Rev. B **50**, 8911 (1994).
 - ⁵⁴ G. Burns and A.M. Glazer, *Space Groups for Solid State Scientists*, Academic Press 1978.
 - ⁵⁵ W. Zhong, R. D. King-Smith and D. Vanderbilt, Phys. Rev. Lett. **72**, 3618 (1994).
 - ⁵⁶ C. LaSota, C-Z Wang, R. Yu, and H. Krakauer, Ferroelectrics **194**, 109 (1997).

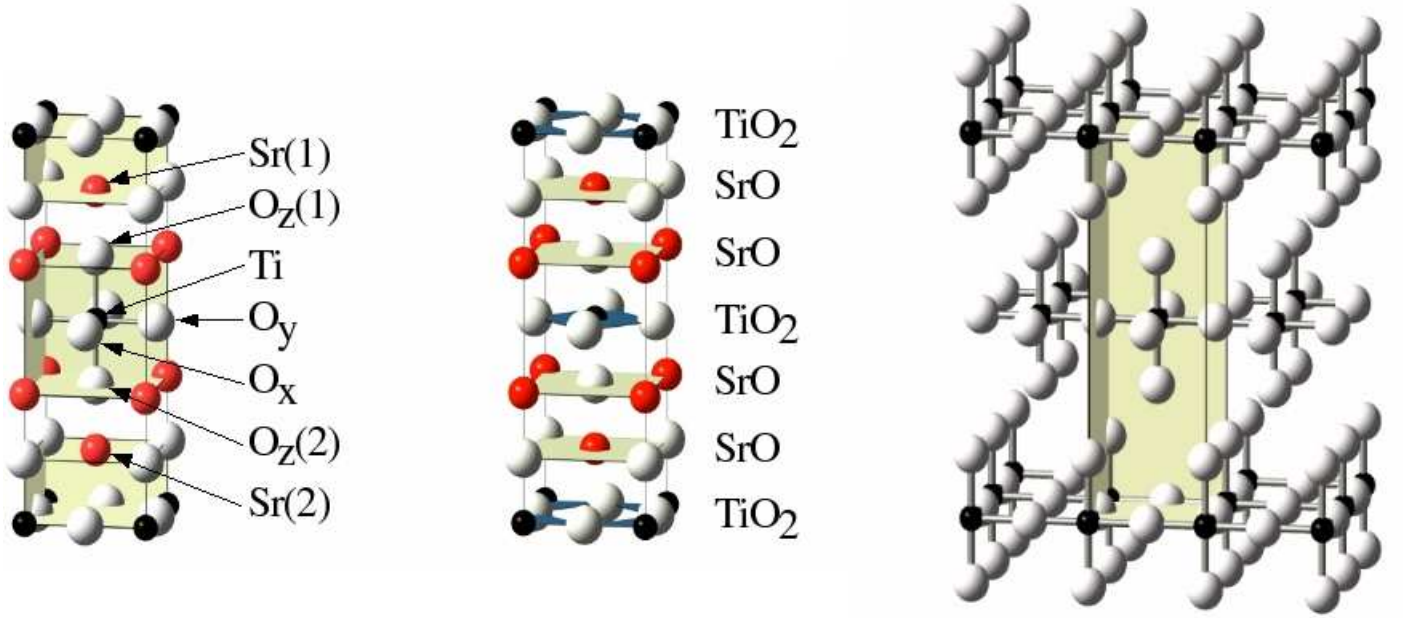


FIG. 1: (Color online) The structure of Sr_2TiO_4 (space group $I4/mmm$) can be viewed as (a) a stacking of SrO-terminated SrTiO_3 perovskite [001] slabs, (b) a stacking of TiO_2 and of SrO planes along [001], and (c) a series of Ti-O chains, infinitely long in the plane along [100] and [010], and of finite extent along [001] (the Sr-atoms have been removed for clarity).

TABLE I: Wyckoff positions for Sr_2TiO_4 .

Atom	Wyckoff position and point symmetry	Coordinates
Ti	(2a) $4/mmm$	0,0,0
O_x, O_y	(4c) mmm	$\frac{1}{2}, 0, 0$; $0, \frac{1}{2}, 0$
O_z	(4e) $4mm$	$0, 0, \pm z_{\text{O}_z}$
Sr	(4e) $4mm$	$0, 0, \pm z_{\text{Sr}}$

TABLE II: Structural parameters of Sr_2TiO_4 . (a) Fully relaxed cell. (b) Relaxation along c-axis, with a lattice constant fixed at theoretical SrTiO_3 . (c) Relaxation with lattice constants fixed at values corrected for thermal expansion. (d) Lattice constants fixed at experimental (Ref. 8). Lattice constants, bond lengths, and internal parameters are in Å.

	Experimental			Present Theory				Previous Theory		
	Ceramic ^a	Ceramic ^b	Thin Film ^c	(a)	(b)	(c)	(d)	Ref. 34 ^d	Ref. 35 ^e	Ref. 36 ^f
Lattice Constants										
a	3.88	3.88	3.88	3.822	3.846	3.855	3.88	3.942	4.0	3.892
c	12.60		12.46	12.32	12.27	12.30	12.46	12.56	12.68	12.70
c/a	3.247		3.211	3.223	3.190	3.190	3.211	3.186	3.17	3.263
Bond Lengths										
Ti-O _x		1.94		1.911	1.923	1.928	1.940		2.0	
Ti-O _z		1.92		1.967	1.960	1.962	1.974		2.0	
Sr-O _z		2.56		2.402	2.397	2.406	2.455		2.47	
Internal Parameters										
δ_{SrO}				0.176	0.182	0.180	0.173		0.12	
u'				1.879	1.869	1.872	1.888		1.94	
v				2.402	2.397	2.406	2.455		2.47	
Reduced Coordinates										
z_{Oz}				0.160	0.160	0.160	0.158		0.158	
z_{Sr}				0.355	0.355	0.355	0.355		0.353	

^aRef. 1,2,3,4

^bRef. 52

^cRef. 8

^dab initio, DFT, GGA

^esemiempirical Hartree-Fock

^fempirical atomistic simulations

TABLE III: Nonzero components of the calculated Born effective charge tensors Sr_2TiO_4 .

Atom	(a)			(b)			(c)			(d)		
	Z_{xx}^*	Z_{yy}^*	Z_{zz}^*	Z_{xx}^*	Z_{yy}^*	Z_{zz}^*	Z_{xx}^*	Z_{yy}^*	Z_{zz}^*	Z_{xx}^*	Z_{yy}^*	Z_{zz}^*
Ti	6.96	6.96	5.14	6.89	6.89	5.20	6.88	6.88	5.20	6.88	6.88	5.15
O _y	-2.04	-5.46	-1.56	-2.05	-5.40	-1.55	-2.04	-5.40	-1.55	-2.04	-5.42	-1.52
Sr	2.37	2.37	2.75	2.36	2.36	2.76	2.36	2.36	2.75	2.37	2.37	2.72
O _z	-2.09	-2.09	-3.74	-2.08	-2.08	-3.79	-2.07	-2.07	-3.78	-2.08	-2.08	-3.75

TABLE IV: Phonon frequencies (cm^{-1}) and mode assignments for Sr_2TiO_4 . Symmetry labels follow the convention of Ref. 54. Experimental values are from Ref. 41.

Mode	Expt.	(a)	(b)	(c)	(d)
Raman					
A_{1g}	205	216	217	214	200
A_{1g}	578	588	594	588	562
E_g	124	121	118	115	106
E_g	286	271	268	266	263
Infrared					
A_{2u} (TO1)	242	231	231	227	206
A_{2u} (TO2)		378	391	389	368
A_{2u} (TO3)	545	499	501	496	478
A_{2u} (LO)		252	253	249	233
A_{2u} (LO)	467	479	482	480	472
A_{2u} (LO)	683	684	692	687	658
E_u (TO1)	151	148	134	129	117
E_u (TO2)	197	218	211	208	198
E_u (TO3)	259	246	247	244	230
E_u (TO4)		611	590	581	554
E_u (LO)	182	184	180	177	168
E_u (LO)	239	227	225	223	216
E_u (LO)	467	451	450	448	443
E_u (LO)	727	789	766	756	727
Silent					
B_{2u}		303	310	310	303

TABLE V: Dynamical matrix eigenvectors, ξ_m , of Sr_2TiO_4 for the fully relaxed structure with $a=3.822\text{\AA}$ and $c=12.32\text{\AA}$. The corresponding eigendisplacement in real space can be obtained by dividing each value by the appropriate mass factor $\sqrt{M_i}$. Modes A_{1g} , A_{2u} , and B_{2u} involve motion along $[001]$, while the two-fold degenerate modes E_g and E_u involve motion along $[100]$ and equivalently along $[010]$.

		Eigenmodes						
Mode	Frequency	Ti	O _y	O _x	Sr(1)	Sr(2)	O _z (1)	O _z (2)
Raman								
A _{1g}	216	0	0	0	-0.71	0.71	0.03	-0.03
A _{1g}	588	0	0	0	-0.03	0.03	-0.71	0.71
E _g	121	0	0	0	-0.70	0.70	-0.06	0.06
E _g	271	0	0	0	0.06	-0.06	-0.70	0.70
Infrared								
A _{2u} (TO1)	231	0.48	0.38	0.38	-0.44	-0.44	0.23	0.23
A _{2u} (TO2)	378	-0.77	0.29	0.29	0.01	0.01	0.34	0.34
A _{2u} (TO3)	499	0.11	-0.46	-0.46	-0.07	-0.07	0.53	0.53
E _u (TO1)	148	0.14	0.11	0.24	-0.37	-0.37	0.56	0.56
E _u (TO2)	218	-0.77	-0.29	-0.14	0.24	0.24	0.31	0.31
E _u (TO3)	246	0.45	-0.86	-0.19	0.02	0.02	0.09	0.09
E _u (TO4)	611	0.16	0.32	-0.91	0	0	0.14	0.14
Silent								
B _{2u}	303	0	0.71	-0.71	0	0	0	0

TABLE VI: Effective plasma frequency, $\Omega_{p,m}$ (cm^{-1}), and mode contribution to the static dielectric tensor, $\Delta\epsilon_m$, in Sr_2TiO_4 .

	(a)		(b)		(c)		(d)	
Mode	$\Omega_{p,m}$	$\Delta\epsilon_m$	$\Omega_{p,m}$	$\Delta\epsilon_m$	$\Omega_{p,m}$	$\Delta\epsilon_m$	$\Omega_{p,m}$	$\Delta\epsilon_m$
$A_{2u}(\text{TO1})$	457	3.93	446	3.71	449	3.93	474	5.28
$A_{2u}(\text{TO2})$	1061	7.86	1066	7.42	1073	7.62	1083	8.66
$A_{2u}(\text{TO3})$	427	0.73	447	0.80	409	0.68	232	0.24
$E_u(\text{TO1})$	752	25.9	809	36.44	829	41.00	888	57.24
$E_u(\text{TO2})$	473	4.69	491	5.41	507	5.95	586	8.80
$E_u(\text{TO3})$	794	10.4	745	9.08	723	8.78	617	7.21
$E_u(\text{TO4})$	812	1.77	759	1.65	737	1.61	674	1.48

TABLE VII: Nonzero components of the electronic and the ionic dielectric tensors for Sr_2TiO_4 , $(\epsilon_{xx}, \epsilon_{yy}, \epsilon_{zz})$. Experimental measurements on thin films (Ref. 9) and on ceramic samples (Ref. 4,5,7) were conducted at room temperature except for \dagger (T=15K.)

	Experimental				(a)	(b)	(c)	(d)
	Ref. 9	Ref. 7	Ref. 4	Ref. 5				
ϵ^∞					(5.09 5.09 4.81)	(5.08 5.08 4.82)	(5.07 5.07 4.82)	(5.08 5.08 4.79)
ϵ_{ionic}					(42.8 42.8 12.5)	(52.6 52.6 11.9)	(57.3 57.3 12.2)	(74.7 74.7 14.2)
ϵ_0					(48 48 17)	(58 58 17)	(62 62 17)	(80 80 19)
$\epsilon_{\text{average}}$	44 ± 4	38	34, 37 †	37	38	44	47	60

TABLE VIII: The structural and dielectric properties of SrTiO_3 calculated within present theory. (6x6x6 grid, 45 Ha.)

Lattice Constant	Phonons (cm^{-1})	ω_m	$\Omega_{p,m}$
$a = 3.846 \text{ \AA}$	$A_{2u}(\text{TO1})$	103	1275
Born Effective Charge	$A_{2u}(\text{TO2})$	189	827
$Z^*(Ti) = 7.26$	$A_{2u}(\text{TO3})$	587	946
$Z^*(Sr) = 2.55$	$A_{2u}(\text{LO1})$	166	
$Z^*(O_\perp) = -2.04$	$A_{2u}(\text{LO2})$	451	
$Z^*(O_\parallel) = -5.72$	$A_{2u}(\text{LO3})$	822	
Dielectric Constant			
$\epsilon^\infty = 6.2, \epsilon_0 = 181$			
Phonon Eigenvector	$\{ u_{Ti}, u_{Sr}, u_{O\parallel}, u_{O\perp}, u_{O\perp} \}$		
$A_{2u}(\text{TO1})$	$\{-0.51, -0.14, 0.37, 0.54, 0.54\}$		